



Interpolation of diffusion weighted imaging datasets



Tim B. Dyrby ^{a,*}, Henrik Lundell ^a, Mark W. Burke ^b, Nina L. Reislev ^a, Olaf B. Paulson ^{a,c}, Maurice Ptito ^{a,d,e}, Hartwig R. Siebner ^a

^a Danish Research Centre for Magnetic Resonance, Centre for Functional and Diagnostic Imaging and Research, Copenhagen University Hospital Hvidovre, Hvidovre, Denmark

^b Department of Physiology and Biophysics, Howard University, Washington, DC, USA

^c Neurobiology Research Unit, Copenhagen University Hospital, Rigshospitalet, Copenhagen, Denmark

^d School of Optometry, University of Montreal, Montreal, Canada

^e Department of Neuroscience and Pharmacology, Copenhagen University, Copenhagen, Denmark

ARTICLE INFO

Article history:

Accepted 3 September 2014

Available online 16 September 2014

Keywords:

Cortical layers

Hippocampus

Histology

Diffusion MRI

DTI

Tractography

Validation

Regularisation

Image resolution

ABSTRACT

Diffusion weighted imaging (DWI) is used to study white-matter fibre organisation, orientation and structural connectivity by means of fibre reconstruction algorithms and tractography. For clinical settings, limited scan time compromises the possibilities to achieve high image resolution for finer anatomical details and signal-to-noise-ratio for reliable fibre reconstruction. We assessed the potential benefits of interpolating DWI datasets to a higher image resolution before fibre reconstruction using a diffusion tensor model. Simulations of straight and curved crossing tracts smaller than or equal to the voxel size showed that conventional higher-order interpolation methods improved the geometrical representation of white-matter tracts with reduced partial-volume-effect (PVE), except at tract boundaries. Simulations and interpolation of ex-vivo monkey brain DWI datasets revealed that conventional interpolation methods fail to disentangle fine anatomical details if PVE is too pronounced in the original data. As for validation we used ex-vivo DWI datasets acquired at various image resolutions as well as Nissl-stained sections. Increasing the image resolution by a factor of eight yielded finer geometrical resolution and more anatomical details in complex regions such as tract boundaries and cortical layers, which are normally only visualized at higher image resolutions. Similar results were found with typical clinical human DWI dataset. However, a possible bias in quantitative values imposed by the interpolation method used should be considered. The results indicate that conventional interpolation methods can be successfully applied to DWI datasets for mining anatomical details that are normally seen only at higher resolutions, which will aid in tractography and microstructural mapping of tissue compartments.

© 2014 The Authors. Published by Elsevier Inc. This is an open access article under the CC BY-NC-ND license (<http://creativecommons.org/licenses/by-nc-nd/3.0/>).

Introduction

Practical restrictions in the available scanning time impose major constraints on clinically applied diffusion weighted imaging (DWI) in terms of image resolution and signal-to-noise ratio (SNR). A large voxel size and under-sampled data sets hamper robust fibre and tract reconstruction. Severe partial volume effects (PVE) in the reconstruction render it difficult to correctly resolve crossing and bending fibres as well as interfacing fibre bundles. This limits the analysis of microstructural features e.g. diffusion tensor analysis and reliability of tractography (Oouchi et al., 2007).

Several super resolution (SR) approaches have been suggested to improve the anatomical detail beyond the resolution of the originally acquired DWI data while maintaining SNR. The main idea behind SR is

to obtain partially overlapping low resolution image volumes of the same object which then are interpolated and combined (reconstructed) to provide a single higher image resolution. Greenspan et al. (2002) acquired multiple image volumes with thick but overlapping slices and could thereby reconstruct thinner slices from the overlapping information while maintaining SNR. Similar attempts have recently been presented where multiple images with anisotropic voxels are acquired with multiple orientations (Poot et al., 2012; Scherrer et al., 2012). Such super resolution methods use adapted acquisition protocols and non-standard reconstruction methods, and can therefore not be applied to already existing DWI data, which limits their use in clinical settings. In contrast to SR techniques, image regularisation techniques do not change the final image resolution of the acquired data. Image regularisation reconstruction techniques use spatial dependence between neighbouring voxels to obtain a more robust result in terms of SNR. For example, in regions with coherent structures such as brain WM fibre bundles, image regularisation is a promising technique for improving the noise properties in DTI (Arsigny et al., 2006; Castaño-Moraga et al., 2004). Interpolation of DWIs is commonly used

* Corresponding author at: Danish Research Centre for Magnetic Resonance, Centre for Functional and Diagnostic Imaging and Research, Copenhagen University Hospital Hvidovre, Denmark. Fax: +45 3647 0302.

E-mail address: timd@drcmr.dk (T.B. Dyrby).

when applying image transformations to align images or when converting DWI datasets acquired with anisotropic voxels to isotropic voxels. Especially, the latter is widely used within the diffusion MRI community when transferring DWI data into a standard space. In contrast to image regularisation techniques, interpolation aims at resampling an image via a transformation to a grid size with higher spatial resolution using an interpolation kernel (Lehmann et al., 1999). Traditionally, interpolation of DWI datasets to higher image resolution has not been thought of as a possible way for potentially increasing anatomical detail in voxel-wise fibre reconstruction. Recently, however, Mai et al. (2011) applied an advanced edge-detection interpolation method with up-sampling of DWI dataset before fitting the diffusion tensor model (Mai et al., 2011). They observed that the fractional anisotropy (FA) map in the up-sampled images seemed to be in geometrical agreement with a reference image acquired at higher resolution. This has been confirmed in other recent studies applying advanced interpolation methods (Coupé et al., 2013; Yap et al., 2014).

In the present study, we applied interpolation to DWI datasets and explored the benefits of interpolation. We expected interpolation to increase anatomical information in both the individual and reconstructed image, revealing finer anatomical details. We used conventional interpolation methods available in most processing toolboxes and investigated the impact of the up-sampling factor on improved image resolution compared to the original image. We assessed the effects of interpolation in four steps. *i*) We used synthetic DWI data from simulated substrates with known tract geometries to investigate the effect of different conventional interpolation methods to reveal anatomical details at various higher image resolutions. Interpolation methods investigated are linear, cubic and 7th-order B-spline methods (Lehmann et al., 1999). *ii*) We used high-quality ex vivo DWI datasets of a fixed Vervet monkey brain that had been acquired on a high-field preclinical MRI scanner, at both ultra-high and low image resolution (Dyrby et al., 2011). The latter was effectively comparable to the resolution of human in vivo data acquired in a clinical setting. The original lower resolution DWI data were interpolated to various higher image resolutions, reconstructed using the diffusion tensor (DT) model (Basser et al., 1994) and compared with the high resolution reference data. *iii*) We performed classical histology on the same regions investigated with DWI data to verify the underlying anatomical features. *iv*) We finally applied our framework to conventional clinical human in vivo DWI data to demonstrate the potential and limitations of interpolating DWI dataset before reconstruction.

Methods

Subjects

Ex vivo monkey brain data

Two healthy adult male Vervet monkeys (*Chlorocebus sabaeus*) were used for this study; one 32 month old for imaging and one 8 year old for histological analysis. The animals were obtained from the Behavioral Science Foundation, St. Kitts and were socially housed in enriched environments. The experimental protocol was reviewed and approved by the Institutional Review Board of the Behavioral Science Foundation acting under the auspices of the Canadian Council on Animal Care.

In vivo human brain data

The human subject was a 28 year old female with no known history of neurological disorders. Oral and written consent were obtained from the subject prior to data acquisition, and MR-scanning procedures were approved by the local ethics committee for Copenhagen and Frederiksberg (ethics protocol number (KF) 01 328 723).

MR scanning

Ex vivo DWI scanning

Ex vivo imaging was performed on an experimental 4.7 T Agilent scanner with a quadrature volume RF coil and maximum gradient strength of 400 mT/m.

The setup followed the preparation stages in Dyrby et al. (2011) where free fixative also was washed out to increase T2-relaxation using phosphate buffered saline (PBS). The brain was placed in a sealed plastic bag with minimal PBS surrounding the brain tissue. Before scanning, the brain was stabilised to room temperature, and placed in the middle of the volume coil using a mechanically stable setup. While scanning, a conditioned flow of air around the fixed brain ensured constant temperature while scanning. The temperature was measured at the end of the magnet ($19 \pm 1^\circ\text{C}$). A DWI pre-scan of 18 h ensured removal of any short-term mechanic and thermal instabilities (Dyrby et al., 2011).

In a single scanning session six whole-brain DWI datasets were acquired in 19 days. A pulse-gradient-spin-echo (PGSE) sequence with single-line readout was used due to its robustness to susceptibility artefacts. We acquired 5 DWI datasets (I–V) with isotropic voxel sizes of 1^3 , 0.8^3 , 0.6^3 , 0.5^3 and 0.4^3 mm 3 (no gap) with whole brain coverage by using 45, 60, 79, 85 and 100 axial slices, respectively. A high resolution DWI dataset (VI) included 50 coronal slices partly covering the brain with in-plane resolution of 0.25×0.25 mm 2 , slice thickness of 0.5 mm and 2 mm gap. The number of excitations (NEX) for DWI datasets I–VI was 1, 1, 2, 4, 8, 8, respectively. To increase SNR the magnitude image volumes for each DWI dataset were averaged off-line. The SNR of a single acquisition in DWI datasets I–VI was 104, 52, 48, 24, 12 and 6 (Gudbjartsson and Patz, 1995). All datasets were acquired with the parameters TR = 5500 ms (but 3200 ms for DWI dataset VI), TE = 47 ms, and each repetition included 3 non-diffusion weighted and 61 non-collinear diffusion weighted directions (Jansons and Alexander, 2003). A b-value of 4056 s/mm 2 for ex vivo imaging was selected (gradient strength G = 180 mT/m, pulse width δ = 8 ms and time between pulse onset Δ = 30 ms) as in Dyrby et al. (2011).

In vivo DWI imaging

In vivo human MRI data were acquired on a 3 T Siemens Verio scanner (Siemens, Erlangen, Germany) with a 32-channel head coil. Seventy-one volumes of whole-brain DWI were acquired in 61 non-collinear directions ($b = 1500$ s/mm 2) and 10 non-diffusion weighted images ($b = 0$ s/mm 2), using the twice-refocused spin-echo sequence (Reese et al., 2003) (TE = 89 ms, TR = 11440 ms, 61 axial slices, isotropic 2.3^3 mm 3 voxels and Grappa = 2, 24 reference lines and 6/8 partial Fourier, NEX = 2). Total scan time for one repetition of the DWI sequence was 14 min. Additionally, a set of reversed phase-encoded $b = 0$ s/mm 2 images was acquired for post acquisition correction of geometrical distortions.

Monkey histology

After euthanasia and thoracotomy, each animal was perfused transcardially with 1.5 L phosphate buffer saline (pH = 7.4), followed by 1.5 L of 4% paraformaldehyde. The brains were extracted, post-fixed overnight in 4% paraformaldehyde and stored in a 1% paraformaldehyde solution until further processing (Burke et al., 2009). The brain for MRI was then prepared for ex vivo imaging as described in Dyrby et al. (2011). The second brain to be used for histological analysis was sectioned and stained (Nissl) by NeuroScience Associates (Nashville, TN). Briefly, the brain was cryoprotected and subbed in a gelatin matrix and sectioned at 40 μm in 24 parallel series. One series of sections were mounted on gelatine-subbed slides and stained for Nissl with thionine. The sections were dehydrated through graded alcohol solutions (50–100%), defatted in a chloroform/ether/alcohol solution, rehydrated and stained in a 0.05% thionine in a 0.08 M acetate buffer (pH = 4.5) for

one minute. The sections were then rinsed, differentiated in a 95% alcohol/acetic acid solution, dehydrated in graded alcohol series (70, 95, 95, 100%), cleared in xylene, and cover slipped with Permount (Fisher Scientific, PA). The Nissl stained sections were then scanned and uploaded into BrainMaps.org (<http://brainmaps.org/>) as part of an ongoing stereotaxic atlas project.

Data processing

Ex vivo monkey data

Visual inspection of the ex vivo data revealed that no additional post-processing in terms of motion correction or eddy currents was needed before further fibre reconstruction as in Dyrby et al. (2011).

In vivo human data

The in vivo human dataset was post-processed in the following processing stages and only one interpolation step was applied. Geometric distortions related to susceptibility artefacts were minimised in the DWIs with the application of a voxel displacement map (VDM) estimated from the two acquired reversed phase encoded $b = 0$ s/mm² images (Andersson et al., 2003; Smith et al., 2004). A full affine transformation between the DWI volumes, using normalised mutual information, was applied to reduce motion and eddy current induced distortions. Finally, the orientation of the 61 non-collinear directions was reoriented according to the orientation introduced by the transformations (Leemans and Jones, 2009).

Finally, transformations were then applied using a 7th-order B-spline interpolation method implemented in the SPM8 toolbox ([url://www.fil.ion.ucl.ac.uk/spm](http://www.fil.ion.ucl.ac.uk/spm)) in Matlab (Mathworks Inc., Natick, USA). Two DWI datasets were generated using different sampling factors (SF); One with SF = 1 hence keeping the original image resolution i.e. 2.3³ mm³, and a second with SF = 8 resulting in a DWI dataset with a final image resolution of 1.15³ mm³.

Fibre-reconstruction

For demonstrating the effects of interpolating DWI datasets, the widely used diffusion tensor (DT) model (Basser et al., 1994) was employed. We used the Camino toolkit with non-linear DT fitting for calculating DTI indices as radial (RD) and axial (AD) diffusivity, and FA maps. For visualisation, the FA maps were Directional Encoded Colour-coded (DEC) using red-green-blue (RGB) colours abbreviated as DEC-FA (Pajevic and Pierpaoli, 1999).

Simulations

Two substrates with simple 3D geometries were constructed for investigating the impact of up-sampling and the interpolation methods employed when using signal components from tracts on sub-voxel length-scales. A two-compartment Gaussian model was used consisting of two interleaving fibre tracts systems. One tract system consists of broader sheet like fibre tracts with through plane anisotropy (Fig. 1a, DEC-FA coloured blue). The other tract system contains thinner tracts with anisotropy in-plane, consisting of vertically straight and curved tracts (Figs. 1b and c, DEC-FA coloured green). In the first substrate with straight fibre tracts, the tract thicknesses were set to $l_t = 0.8, 0.9, 1.0$ and 1.1 relative to the voxel size l of the original low resolution substrate and spaced 7 voxels apart. The tracts were placed along the intersection of two columns of voxels with the first eigenvector oriented vertically exemplifying a worst-case scenario of a PVE (Fig. 1b). In the second substrate with curved tracts, a low-resolution dataset was created from a synthetic high resolution dataset with curved tracts as shown in Fig. 1c. The eigenvalues of the local diffusion tensors were set to the same as in the substrate with straight tracts, but the first eigenvector followed the local tangent. The tract thicknesses were set to $l_t = 0.7, 0.8, 0.9$ and 1 relative to the voxel dimension of the

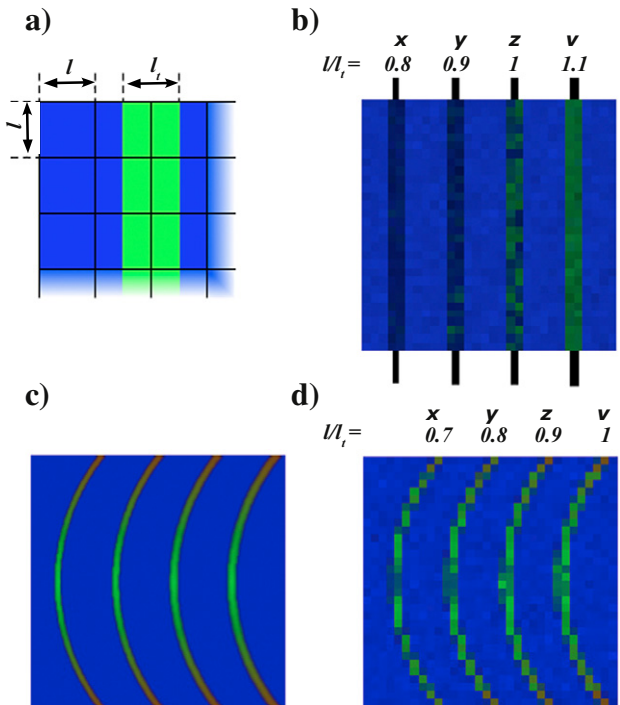


Fig. 1. Simulated substrates of straight and curved fibres with various degrees of partial volume effect (PVE). a) The substrates consist of two interleaving anisotropic fibre systems with orthogonal projections as indicated by the directional encoding colours DEC-FA (blue and green respectively). Voxel size i.e. an isotropic grid size with size l , and l_t is the thickness of a tract. b) Straight fibre substrate with four tracts x, y, z and v having anisotropic in-plane (DEC-FA: green) and increasing relative thickness (l_t/l) compared to the grid size. Between tracts x–v are placed larger tracts with orthogonal projection (DEC-FA: blue). c) Substrates designed as for straight fibres but with curved tracts. c) Curved tracts in high resolution with minimal PVE acting as the truth, and d) downsampled to lower image resolution. For all simulations practical realistic noise levels are added to both straight and curved fibres.

downsampled resolution l , and the fibre tracts were curved with a radius of 26 times the voxel resolution (Figs. 1c, d).

In this way we produced different realistic levels of PVE due to a conflict between limited image resolution (grid size) and tract geometry as the tract thickness i.e. cross-sectional area of the tract, resulting in voxels containing a fraction of both tract systems in Figs. 1b, d. The eigenvalues of the two compartments were identical and set to $\lambda_1 = 5E-10$ m/s² and $\lambda_2 = \lambda_3 = 1E-10$ m/s² that are comparable values found in perfusion fixated Vervet monkey white matter tissue from Lundell et al. (2011). The resulting FA value is 0.68. Synthetic diffusion MRI data was calculated inversely from the constructed geometry using the Camino toolbox (Cook et al., 2006) (<http://cmic.cs.ucl.ac.uk/camino/>) with a SNR of 20 for the 61 gradient directions and b-value as used in the imaging experiments. The simulated substrate was constant in slice direction over the whole width of the interpolation kernel, but the noise was independently modelled in each slice.

Analysis

The sampling factor

We define interpolation and up-sampling to higher image resolution as a sampling factor (SF) being the ratio between the voxel volume of the original (low resolution) image and that of the interpolated. Hence, a sampling factor of 1 means that the original image resolution has not been changed before fibre reconstruction, whereas doubling the image resolution lead to SF = 8.

Synthetic diffusion MRI data analysis

We test how different conventional interpolation methods available as well as the SF impact the anatomical features of the reconstructed image. Synthetic diffusion MRI (linear and curved substrates) was up-sampled to voxel sizes $l_i = 1/2, 1/3$ and $1/4$, corresponding to an SF of 8, 27 and 64 using a linear, cubic and 7th-order B-spline interpolation method, as implemented in the SPM8 toolbox. The B-spline function is given by a linearly weighted combination of basis functions positioned throughout the spatial image domain. The order of the function is determined by the order of the piece-wise polynomial basis functions, where an increasing order results in a larger spatial support region for each basis function. For instance, an order of 1, 3 and 7, results in a spline function value being influenced by at most the $2^d, 4^d$ or 8^d closest voxels of the original image resolution, where d refers to the image dimensionality. A survey of the interpolation methods investigated is covered in Lehmann et al. (1999). We investigated how the SF impacts the DTI indices and the shape of the tensor via the MODE index ranging from -1 for oblate to 1 for linear anisotropic (Kindlmann et al., 2007).

Diffusion MRI data

For each of the ex vivo datasets acquired with different original image resolutions, several sampling factors were applied corresponding to a range of interpolated image resolutions ranging from $0.8^3, 0.6^3, 0.5^3, 0.4^3$ to 0.25^3 isotropic mm 3 . We used the interpolation method that demonstrated the best performance in the analysis based on synthetic diffusion MRI data.

A quantitative analysis of the effect of interpolation was performed using the 0.4^3 mm 3 DWI dataset as high resolution gold standard. The high resolution dataset was down-sampled to a 0.8^3 mm 3 low resolution dataset using nearest neighbour interpolation. The high and low resolution datasets were then reconstructed in five different ways to evaluate error in FA and principal direction estimates. (i) DT reconstruction of the original high resolution gold standard dataset. (ii) DT reconstruction of the FA image of the low resolution dataset i.e. no change in effective image resolution and (iii) 7th-order B-spline interpolation of the scalar FA image calculated from the low resolution dataset. (iv) 7th-order B-spline interpolation of the low resolution DT elements with subsequent eigenvector estimation and FA calculation. The latter was done with a log-Euclidean transformation to satisfy the relation between the DWI signal and the tensor elements (Arsigny et al., 2006). (v) 7th-order interpolation of the low resolution DWI to high resolution and then DT reconstruction. Maps of absolute error in FA and angular deflection of the principal direction from the gold standard to the high resolution dataset (i) were computed for the datasets with low resolution origin (ii–v). To allow voxel-wise comparison, the low resolution dataset (ii) was interpolated to high resolution using nearest neighbour interpolation.

Results

Simulations

Original image resolution

Straight fibre tracts that fill up less than 100% of a voxel as seen for tract x, y and z in Fig. 1b (DEC-FA displayed in green) showed decreasing FA values due to the increasing PVE from the neighbouring broader fibre tracts with larger cross-section (Fig. 1b, DEC-FA displayed in blue). Lower FA values were continuously observed along the broader tract v , but PVE renders its cross-sectional area twice as broad (two voxels) compared to the original tract in Fig. 1a. All fibre tracts ($x-v$) displayed similar PVE-induced “broadening” because their geometrical dimensions did not fit the grid size used for sampling.

Sampling factor

For the interpolation methods in Fig. 2, increasing the SF resulted in an overall improved reconstruction of straight fibre tracts ($x-v$) when compared with the original image shown in Fig. 1b. The tracts displayed a more consistent direction (green colour) along the whole tract. Most improvement was observed for a SF of 27 and higher. At a SF of 27 or higher, the principal direction started to emerge even for the thinnest tract v . In agreement with the true tract in Fig. 1a, the principal direction became more dominant (labelled in green in DEC-FA) instead of showing low anisotropy as in Fig. 1b. This indicates that the adverse effects of PVE on the directionality of fibre tracts gradually diminished at higher SF.

The geometry of the reconstructed tracts was also positively affected by the applied interpolation method, but the success depended on the thickness of the true underlying tracts: using 1st-order B-spline, the reconstructed fibre tracts y, z and v appeared to have similar thickness for any SF. However, when using 7th-order B-spline, reconstruction yielded increasing tract thickness for tract x, y, z and v and thus, appropriately reflected the true thickness of the tracts as shown in Fig. 1b. A similar tendency was observed when comparing the 3rd- and 7th-order B-spline results, albeit revealing a much weaker effect. For the 7th-order B-spline, the main contour of tract v and z tended to be thinner but the boundary along the tract appeared to be noisy (piecewise broader), which might be related to the relative low SNR of 20 used. The geometry effects are also displayed in Figs. 2b, c where the mean FA, mean RD and AD were calculated within each column of the images when using 7th-order B-spline interpolation with SF of 1 (black) and 64 (red). The interpolated high resolution substrates showed improvements in how many samples (equal a distance) that represent the thickness of a tract: the broader the original tract (i.e. from tract x to v) the broader the reconstructed tract. This was the case for high SF of 64 but not for low SF of 1 where the tract thickness was unchanged.

The line profiles displayed in Figs. 2b, c show no significant changes in mean anisotropy (FA), RD or AD for any SF or interpolation method within ROIs of the tracts, yet spatial differences can be observed. First, for reconstructed interpolated datasets in Fig. 2a a thin band of low FA values appears all along the boundary between the two tract systems. This suggests increased PVE after interpolation, which is likely due to the detection of two crossing fibres tract systems. Secondly, Figs. 2b, c show that FA, RD and AD in the core of especially tracts z and v converge towards the true anisotropy and diffusivities (striped lines) at higher SF. The ringing in Figs. 2b, c originates from reconstructing sharp borders using higher order B-spline interpolation and appears at each side of the transition as an over- or under-shoot that fades out with distance. The frequency of the ringing is determined by the grid size of the original image and not to the final image resolution, i.e. the chosen SF. No ringing is seen for 1st-order B-spline because it is a linear fit between neighbouring voxels (result not shown).

For the remaining analysis, we used 7th-order B-spline interpolation, because this method was amongst the best performing interpolation methods, resulting in the most optimally reconstructed geometry of the true simulated tracts.

Curved fibre tracts

Higher SF (>1) had similar effects on curved fibre tracts as observed for straight fibres as shown in Figs. 3a, b. The geometrical representation of the tract thickness generally followed the representation of the true underlying tract (Fig. 1c), and PVE appeared consistently as low FA values along the boundary between the two tracts. However, the curvature of the tracts introduced general challenges with respect to reconstruction:

The tract midline: For SF = 1, the tracts appeared to be interrupted in curved regions with low FA and MODE values as shown in Figs. 3a, e and for the midline profile for tract x shown in Figs. 3d, h (red line).

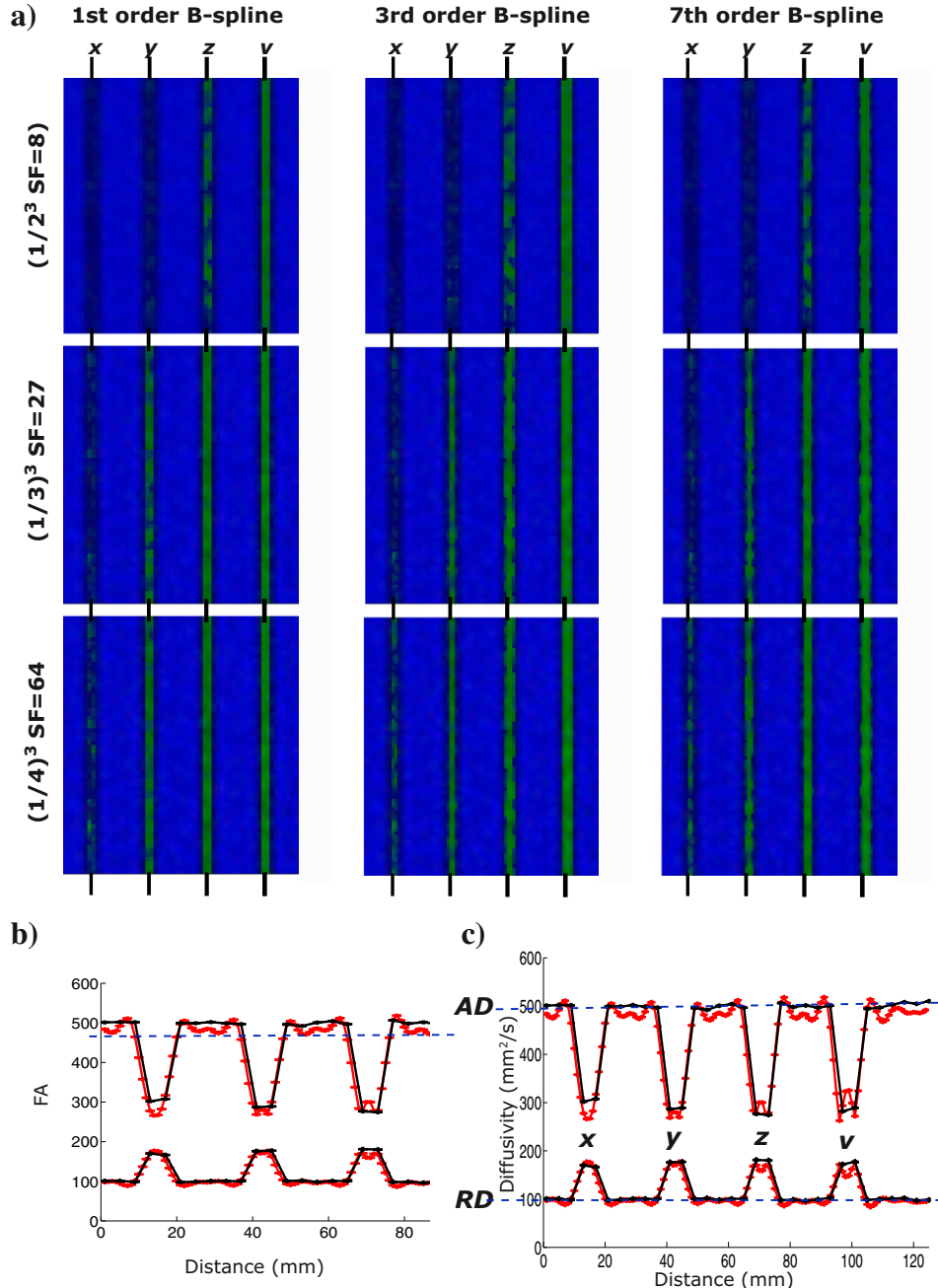


Fig. 2. The effect of interpolation methods and sampling factor on simulated straight fibre tracts x–v (DEC-FA: green) interleaved between orthogonally projecting and larger tracts (DEC-FA: blue) from Fig. 1. a) Columns show DEC-FA results when applying three different interpolation methods to the DWI dataset of straight fibre substrate; from left: 1st-, 3rd- and 7th-order B-spline were used. Rows show increasing sampling factor (SF). b) Fractional anisotropy (FA), c) axial diffusivity (AD) and radial diffusivity (RD) are calculated as the mean of all the voxels within each image column when using 7th-order B-spline with SF of 1 (black) and 64 (red). The x-axis shows the normalised distance of mean values starting from the first left-most image column of the substrates. In b) and c) are true FA, AD and RD values indicated as dashed lines and are the same for all tracts x–v. Due to PVE the location of fibre tracts x–v clearly appears in b) and c) as lowered FA and AD values, and increased RD. The DTI indices for the broader orthogonally projecting tracts are similar to the true values. Crosses indicate where the tract has been sampled i.e. the image resolution.

For SF = 64, clusters of the locally higher FA and MODE values now clearly appeared as “hotspots” in Figs. 3b, f. The “hotspots” appeared systematically along the midline of all the curved tracts. The hotspots indicate the position where the true underlying tracts are optimally represented on the grid in the original image resolution also seen as a correspondence in the oscillations of the midline profiles in Figs. 3d, h. No significant differences in FA or MODE values were found along the midline profile for high SF Figs. 3d, h (red versus blue lines). However, FA values often tended to be higher, while MODE remained unchanged.

The tract geometry: The horizontal profiles (dashed) in Figs. 3a, e, and f and corresponding voxel intensities shown in Figs. 3c and g demonstrate the same increased PVE effects along the boundary between tracts as seen for the straight fibres in Fig. 2b: the appearance of low FA values and negative MODE values. Negative MODE values in Fig. 3b are reflecting oblate tensor shapes that suggest PVE caused by two orthogonally crossing fibres tracts. Ringing artefacts mimicking the shape of the curved tracts are also clearly seen in the interpolated FA map as well as in the horizontal FA profile in Figs. 3c, g. The artefact originates from high-order

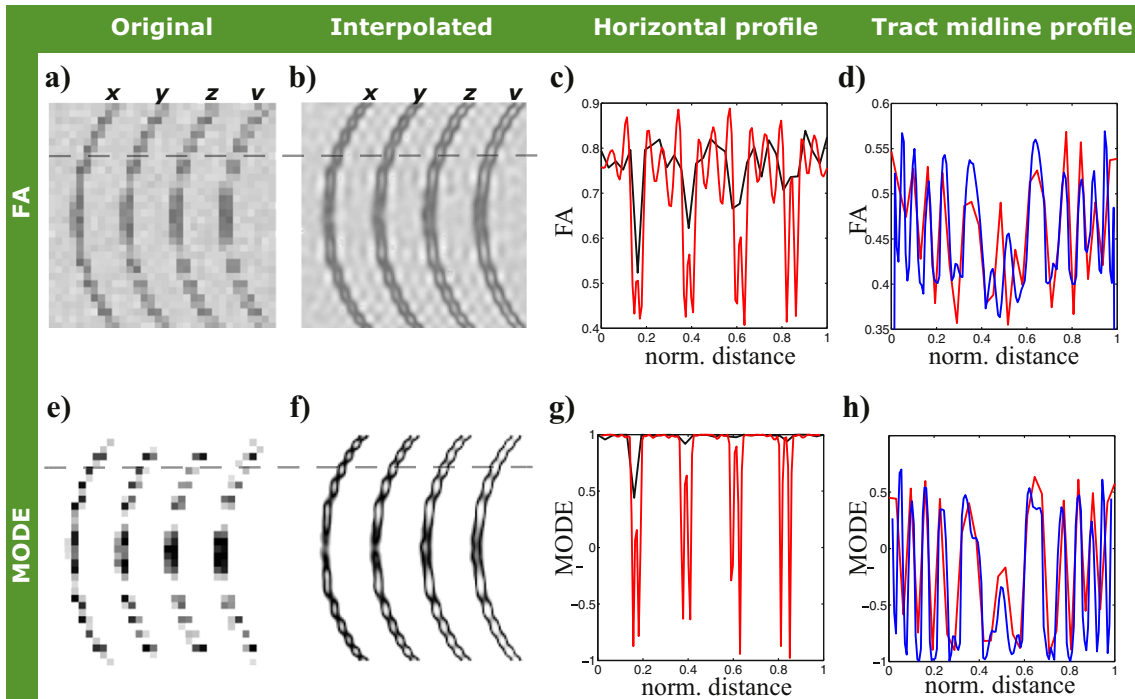


Fig. 3. The effects of sampling factor on simulated curved fibre tracts $x-v$ (DEC-FA; green in Fig. 1) interleaved between orthogonally projecting tracts (DEC-FA; blue in Fig. 1). Results are shown in grey-scale to distract from the directional information of tracts. The 7th-order B-spline interpolation method was used with SF of 1 a), e) and 64 b), f). Results are displayed in FA values c)–d) and MODE e)–h). The line profile following the horizontal dashed line of FA and MODE values shown in a), b) and e), f) are shown in c) and g) as single voxel intensities along the line profile with SF = 1 (black) and for SF = 64 (red) d), h). The tract midline profile of the curved tract x and tract v as a function of normalised distance is shown in d) for FA and in h) for MODE values with SF = 1 (red) and SF = 64 (blue). The true FA value in c) is 0.8 and is the same for all tracts $x-v$, but due to PVE, decreased FA is found at locations where tracts $x-v$ are found along the dashed line profile in a), b) as well as along the tract midline as shown in d) and h).

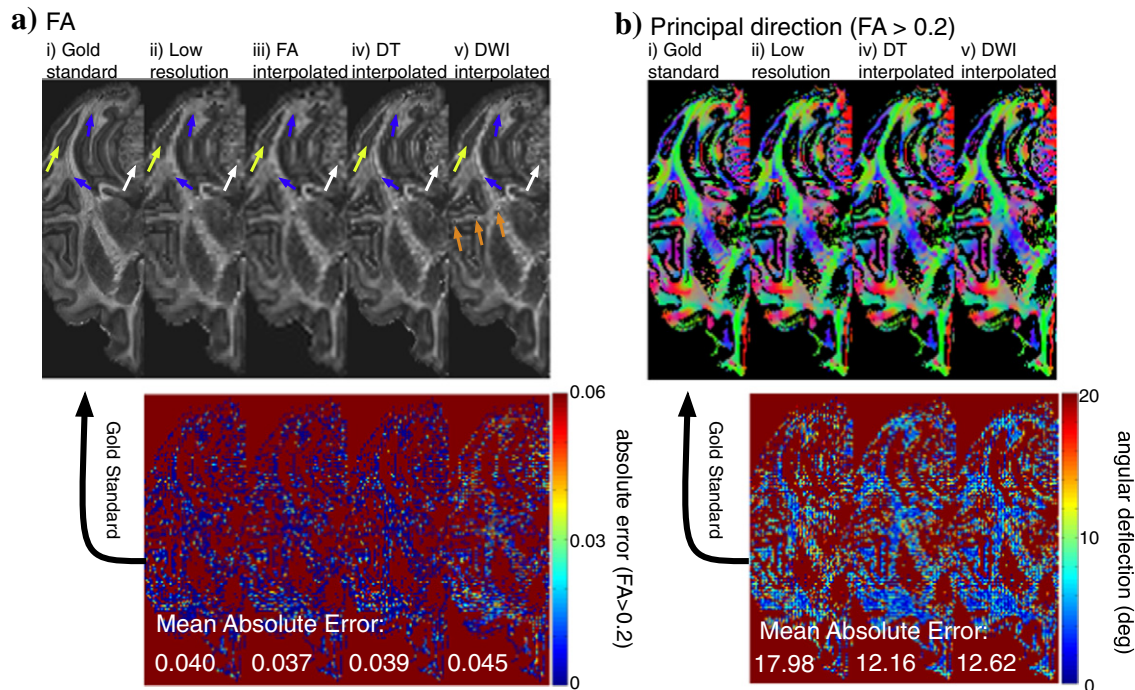


Fig. 4. Quantitative analysis of the effect that different interpolation strategies have on DT reconstruction. Top panels show a) FA and b) principal direction (conventional colour coding, L/R red, A/P green and S/blue) calculated from the original high resolution dataset being the gold standard (i), down sampled low resolution dataset and DT reconstruction of FA image (ii), 7th-order B-spline interpolation of the scalar FA image calculated from the low resolution dataset (iii), interpolated DT metrics (iv) and interpolated DWI data (v). The bottom panels show the corresponding error maps for FA and principal diffusion direction. Mean absolute errors are calculated over anisotropic voxels with $FA > 0.2$ in the original high resolution dataset which served as gold standard. Finer details like cortical layers and layers in the cerebellum (yellow and white arrows) and delineation between different white matter tracts (blue arrows) are visible in the original data (i) and after interpolation of the full tensor or the DWI data (iv and v). Artefacts in the interpolated DWI dataset can be attributed to ringing artefacts (orange arrows).

B-spline interpolation methods when restoring boundaries/edges with systematic spacing. Similar ringing artefacts, although much weaker, also appear in simulations of straight lines as shown in Fig. 2b for SF = 64. From the inspection of the MODE profile in Fig. 3g the ringing artefact appears to have minimal influence on the tensor shape except of a marked under-shoot at tract interfaces.

Ex vivo imaging

A quantitative analysis of how interpolation impacts on FA and principal direction is shown in Fig. 4. Interpolation of low resolution data improved the anatomical detail. Interpolated scalar FA (iii) and tensor (iv) yielded slightly better results than interpolation of DWI data (v) in terms of decreased mean absolute error (Figs. 4a and b). However, some anatomical details, such as cortical layers and delineation of different white matter pathways, were only visible with interpolation of the full tensor or the DWI data but not after interpolation of the reconstructed FA (white, blue and yellow arrows in Fig. 4). Artificially

high FA values (indicated by orange arrows in panel v of Fig. 4a) can be explained by severe ringing artefact after interpolation in regions with high contrast.

Visual inspection of interpolated DWI datasets and DEC-FA in Fig. 5 revealed the similar positive effects for increasing sampling factor as found in the simulations i.e. geometrical representation and directional. An example is the cross-sectional size of the mid-sagittal corpus callosum that for low resolution images appear thin (~1 mm) (Fig. 5g) but with SF it increases in size and appears also geometrically similar to that in the high image resolution images (~1.8 mm) in Fig. 5a. Similarly, better tract representations of thickness were also observed in the simulations. As for the simulations, no significant difference in mean FA values emerged when comparing original and interpolated image resolutions in hippocampus, centrum semiovale, corpus callosum or cortical GM regions. We constructed a histogram of signal intensities from a large ROI drawn in the background of the $b = 0 \text{ s/mm}^2$ images from the 1^3 mm^3 DWI dataset. The histogram showed that the noise profile did not change with interpolation and SF when using 7th-order B-spline.

No obvious hotspot was seen within curved fibre regions such as the hippocampus folding, as was observed in simulations of curved tracts (anatomical label 1). Furthermore, interpolation-related ringing effects, as observed in simulations, were not visible. However, ringing artefacts emerged in larger homogeneous regions, yet they only appeared close to edges i.e. near ventricle (not shown). We attribute these ringing artefacts to Gibbs ringing (an imaging artefact due to limited matrix size) rather than to interpolation. However in the CC, some (single) voxels showed altered directional orientation and FA value after interpolation relative to other voxels in CC (Fig. 5j, arrow). This could be related to an interpolation ringing artefact.

Overall, visual inspection of Fig. 5 suggests that the achievable benefits in terms of anatomical details obtained with various SF depend on the original image resolution and the size of the anatomical structures:

Lower original image resolutions ($>0.6^3 \text{ mm}^3$) are shown in Figs. 5g–j. The improvement of the anatomical contrast between larger white matter structures at higher SFs is paralleled by an overall blurring when compared to the corresponding original higher-resolution images (see Supplemental Fig. S1 for all image resolutions acquired). The blurring effect likely originates from the interpolation method (i.e. kernel applied to individual measurements of the DWI dataset) and insufficient effective resolution in relation to finer anatomical structures (Figs. 5h, i, j versus d, b, a). Overall, improved contrast can be observed for the larger anatomical WM and GM structures in Fig. 5j versus 5g and indicated with anatomical labels 3, 6, 7 and 8. The improved contrast typically results from improved directional information (principle direction of the tensor) and from lower FA values due to PVE at the tract interfaces as also seen in simulations (Figs. 2b, c, SF = 64). Finer details such as the separation of the hippocampal layers remain concealed (Figs. 5h–j, anatomical label 1). Nevertheless, even for the lowest original image resolution of 1^3 mm^3 , higher SF (≥ 4.6) clearly disclose two cortical rims, an inner rim with low FA values, and an outer rim with higher FA values. Especially the outer rim has an orientation, which is generally orthogonal to the cortical surface. This microstructural feature of the cortex can also be seen at the higher original image resolution (Fig. 5, arrows).

For higher original image resolutions ($\leq 0.6^3 \text{ mm}^3$) shown in Figs. 5a–f, the blurring effect was reduced and the contrast between finer anatomical details emerged with increasing SF, resulting in improved geometrical representation and higher appearing resolution. For higher SF (>8), curved-shape structures and their orientation such as the folding of hippocampal layers followed those of the original higher image resolution (Fig. 5, f versus a, anatomical label 1) (see Supplemental Material Fig. S1 for all image resolutions acquired). In addition, the contrast at the boundaries between white matter tracts appeared sharper at higher SF, and the boundary appears spatially continuous

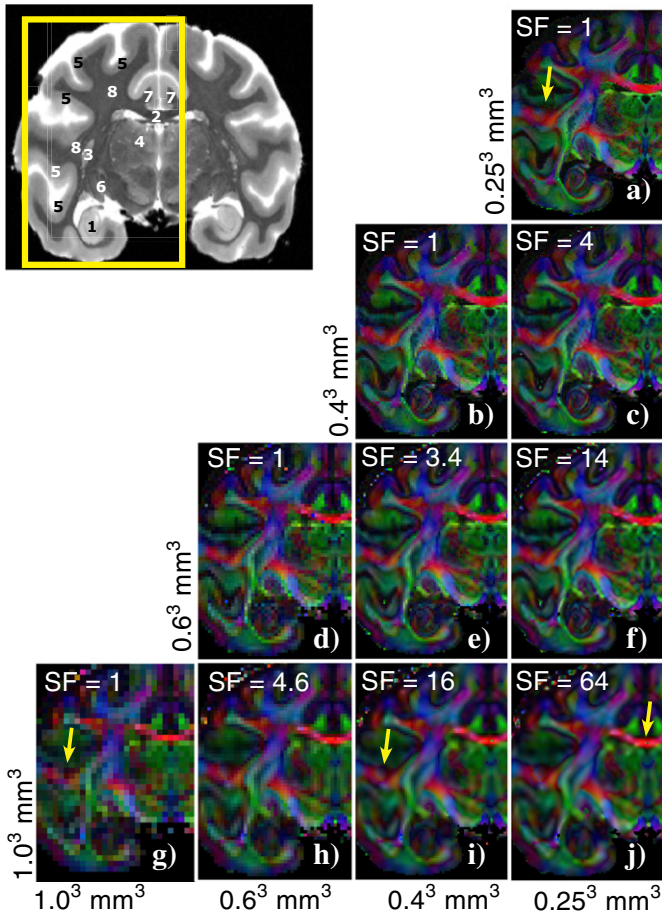


Fig. 5. DTI reconstructions of DWI datasets acquired in various image resolutions with and without prior interpolation and different sampling factors (SF) a–j. Each row show from left first the original image resolution i.e. SF = 1 a), b), g) and d) followed by interpolation with different SF > 1 except for a) the highest image resolution. Note that the highest resolution image in a) has no isotropic voxels but 0.5 mm slice thickness. Top-left corner: $b = 0 \text{ s/mm}^2$ image with indication of the zoomed region (yellow frame) shown in a)–j) where DEC-FA are visualised in RGB colours that indicates the principle direction of the diffusion tensor: right-left (RED), anterior-posterior (GREEN) and ventral-inferior (BLUE). (See Supplemental Fig. S1 for all image resolutions acquired). The arrows indicate an example in cortex where rims of low and higher FA values are seen in i) at interpolated images with SF = 16 as in a) for higher original resolutions but in g) are hard to distinguish at the low image resolution. Anatomical labels in $b = 0 \text{ s/mm}^2$ image indicates: 1: The hippocampus, 2: corpus callosum, 3: putamen, 4: thalamus, 5: cortex, 6: lateral geniculate nucleus, 7: cingulum tract, and 8: centrum semiovale.

as seen for e.g. the centrum semiovale region in Figs. 5(e, f versus a, anatomical label 8). For deeper grey matter regions such as thalamus, caudate nucleus, geniculate nucleus, the contrast to anatomical details was not improved at any original image resolution or higher SF (Figs. 5f, c versus a) (anatomical labels 3, 4, 6).

For SF higher than 16, we observed no further improvement in anatomical details for 1.0^3 and 0.8^3 mm 3 image resolution. For the higher image resolutions with a voxel size of 0.4^3 mm 3 (Fig. 5c), we were not able to observe an improvement for SF > 4 because the highest acquired image resolution is $0.25 \times 0.25 \times 0.5$ mm 3 (Fig. 5a). Nevertheless, isotropic 0.4^3 mm 3 resolution with SF of 4 appeared visually similar to the highest in-plane image resolution.

Interface between cortical grey and subcortical white matter

In addition to WM regions showing PVE caused by interfacing tracts, the interface between GM (high cell density) and WM (high axon density) regions will benefit from interpolation. This can be seen in cortical regions such as the hippocampus (Fig. 5), but the effect is most prominent in the cerebellum. Fig. 6 shows an example for the cerebellum with an original image resolution of 0.5^3 mm 3 (Fig. 6b) and interpolated to 0.25^3 mm 3 (SF = 8, Fig. 6d). After interpolation, DEC-FA revealed a spatially coherent and continuous structural folding of the cortical surface, not seen at the original image resolution (Fig. 6c versus 6a). The contrast may come from the thick and densely packed granular layer in the cerebral cortex (isotropic diffusion) and its interface to two anisotropic structures, namely WM and dendrites in the lower cortical layers as well as parallel fibres in the molecular layer. This contrast between WM and GM already emerged in the individual interpolated images and not only in the reconstructed DTI as shown in Figs. 6b, d.

Anatomical comparison with Nissl staining

Fig. 7 shows a coronal Nissl stained slice of a Vervet brain. The section is positioned to optimally match the DTI image in Fig. 5. Because the Nissl stain is showing cell bodies and DTI is related

to fibre anisotropy and orientation, the two modalities generally have opposite contrast mechanisms. The folded hippocampal layers observed with DTI in Fig. 5a are clearly outlined in the Nissl stain and show consistent folded layers with different cell densities. High cell densities can be found in hippocampal regions CA1-3 and dentate gyrus (DG) and may constitute layers of lower FA values. The putamen (Pu) and claustrum (Cl) have high cell densities. Accordingly, DTI yielded corresponding areas of low FA values. The claustrum for example appears as a thin stripe (few voxel broad) of low FA values (Figs. 5a, f, j). It was possible to identify the claustrum based on DEC-FA from any original image resolution interpolated to $<0.4^3$ mm 3 (Figs. 5b, e, i). Although the claustrum was not visible at the original 1^3 mm 3 image resolution, it weakly appeared with a SF of 64 (Fig. 5j). The larger putamen also appeared more consistently at higher SFs (Fig. 5g versus j, and d versus f). Yet, when applying a high SF to the low original image resolution, the putamen appeared blurred (Fig. 5g versus j). The blurring of the putamen might be explained by the PVE between GM and the dense WM fibres projecting through the putamen that are clearly seen in the Nissl stain (Fig. 7). While the lateral geniculate nucleus (LGN) shows curved layers of high cell density in the Nissl stain, the layers were not visible at any original image resolution on DEC-FA in Fig. 5.

In vivo imaging of human brain

Fig. 8 illustrates DEC-FA of a typical clinical in vivo human DWI dataset in 2.3^3 mm 3 with and without interpolation (SF = 8). Similar effects of interpolation were reproduced as in the ex vivo monkey data (Fig. 5) and in simulations (Figs. 2 and 3). No ringing effects were visible as in the ex vivo monkey data. A SF = 8 improved contrasts between interfacing fibre tracts as seen in the region of the centrum semiovale where a stripe of low FA values appeared which was not evident at original image resolution (Figs. 8a, b versus c, d, single arrow). Furthermore, the outline of the interface between cingulum and corpus callosum fibres improved and geometrically the thickness of the cingulate appeared more consistent (Fig. 8d, white arrow).

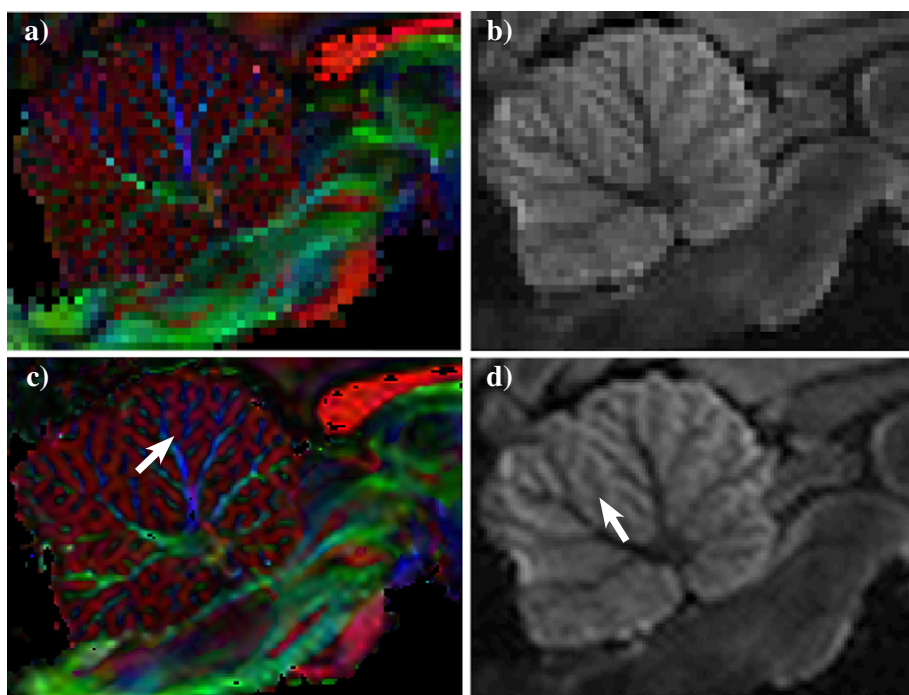


Fig. 6. Sagittal view of the cerebellum showing that improved anatomical details also clearly appear in individual interpolated diffusion weighted images. DWI dataset in original image resolution 0.5^3 mm 3 reconstructed and visualised in a) as DEC-FA, and in b) one of the diffusion weighted image volumes from the DWI dataset. After interpolation to 0.25^3 mm 3 using SF = 64 visualised in c) as DEC-FA and in d) diffusion weighted image volume. Arrows indicate improved geometrical information with interpolation in DEC-FA and diffusivity.

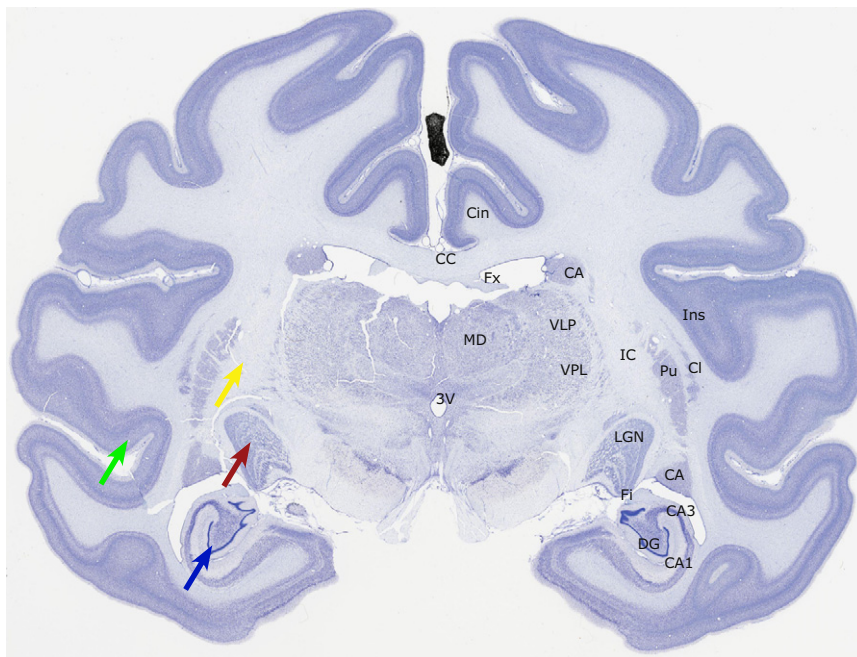


Fig. 7. Nissl stain of the Vervet monkey brain for comparison with anatomical findings with DTI results. The coronal slice is positioned similar to the coronal slice from DTI in Fig. 4. Arrows indicate anatomical regions: Layers in cerebral cortex (green arrow), WM in internal capsule (yellow arrow), layers of lateral geniculate nucleus (red arrow) and the hippocampal CA1-3 region with high cell density in dentate gyrus (blue arrow). Abbreviations: Cin: cingulum bundle, CC: corpus callosum, Ca: caudate, Fx: fornix, MD: medio-dorsal thalamus, VLP: ventra-lateral posterior thalamus, 3V: third ventricle, VPL: ventral-posterior lateral thalamus, Ins: insula, IC: capsule interna, Pu: putamen, Cl: claustrum, Fi: fimbria, LGN: lateral geniculate nucleus, CA1-3: cornu ammonis, and DG: dentate gyrus.

Better contrast was also observed between GM and WM, especially for deep GM structures. For example, the contrast between internal and external capsule WM projections and the putamen was enhanced (Fig. 8d, double arrow). Also, the contrast between thalamic nuclei became more prominent (Fig. 8, circle). Contrast between cortical layers did not appear as clearly as in the ex vivo monkey data. This was the case with and without interpolation. The same was the case for the hippocampus, where interpolation did not improve the anatomical contrast between hippocampal layers. In analogy to the low resolution monkey datasets, the application of high SF blurred the larger anatomical structures.

In agreement with the ex vivo monkey data and simulations, no significant difference in mean FA values between original and interpolated image resolutions were observed in hippocampus, centrum semiovale, corpus callosum or cortical GM regions.

Discussion

Using conventional interpolation methods, we demonstrate that interpolating DWI datasets to a higher image resolution before voxel-wise reconstruction can reveal anatomical details that are normally only seen in datasets acquired at a higher image resolution. A similar benefit in terms of improved anatomical resolution was achieved by model based interpolation using the full DT, but not when interpolation scalar images (i.e. the FA maps). We employed simulations and high-quality and high resolution ex vivo DWI datasets at various image resolutions to validate the performance of interpolation. We also used anatomical information from Nissl stains to assess the quality of the WM/GM contrast (as provided by high/low FA values) with and without prior interpolation. This enabled us to highlight the pros and cons of specific interpolation settings in relation to specific anatomical features.

Supported by simulations, the results show that more fine-grained anatomical features typically appear in regions with complex fibre configurations. In these regions, interpolation improves (i) the geometrical representation of tract shape, (ii) the contrast at boundaries between

tracts, and (iii) directional information of the principle fibre direction. This suggests that interpolation in combination with reconstruction decreases the adverse impact of PVE caused by low image resolution. At the same time, interpolation increased PVE at the boundary between tracts producing a thin line of low FA values including a mixture of both tracts. We found no significant changes in regional anisotropy, but simulations for straight tracts showed that FA tended to improve accompanied by both a RD increase and AD decreases towards true diffusivities.

Since interpolation can be applied to already existing DWI datasets, this approach bears considerable potential for a wide range of DWI based applications ranging from research to practical clinical use. For example in pre-surgical planning DTI tractography is often used to map the displacements of projecting tracts but low image resolution and limited scanning time can potentially compromise the reliability of the tracking results. Additionally, the possibility to improve anatomical resolution is not limited to the DT model as shown here, but could be expanded to multi-fibre models, tractography and possibly to microstructural imaging techniques that are geared to extract more specific microstructural features such as ActiveAx (Alexander et al., 2010; Dyrby et al., 2012; Zhang et al., 2011) and NODDI (Zhang et al., 2012). One should however bear in mind the challenges with interpolation methods. We for example observed a ringing artefact with higher-order B-spline interpolation that can complicate fitting and comprises the finer anatomical details found. However, there exists a wide range of interpolation methods that suppresses such artefacts and therefore, the selected interpolation method plays a key role on its output.

Interpolation of DWI datasets

Higher-order interpolation methods use local information of neighbouring voxel intensities in the original image to predict the shape of boundaries in a higher image resolution (Lehmann et al., 1999). DWI datasets consist of a series of image volumes. Since each volume measures the diffusivity along different encoding

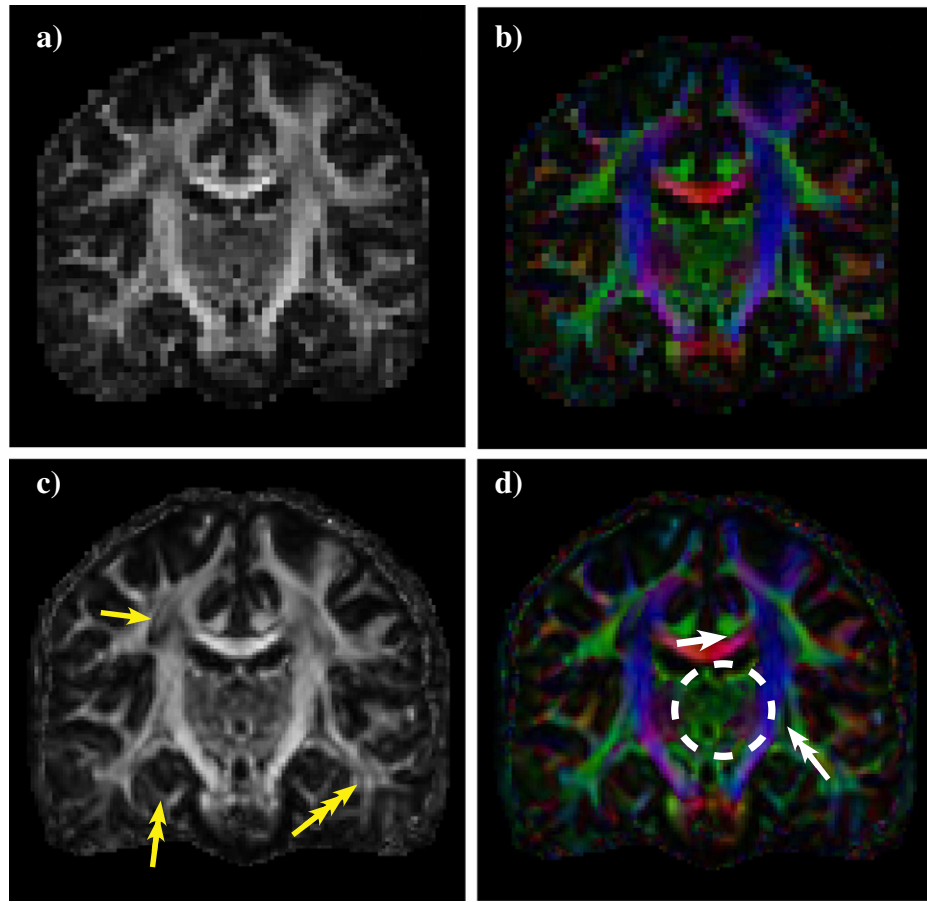


Fig. 8. Coronal view of a typical DTI reconstructed DWI dataset of the living human brain without a), b) and with c), d) interpolation using $SF = 8$ leading respectively to 2.3^3 and 1.15^3 mm^3 isotropic voxels. a), c) Display of FA values and b), d) with DEC-FA. Arrows indicate anatomical regions: c) centrum semiovale (single), hippocampus (double) and parietal WM (triple). In d) the border between the cingulum and corpus callosum fibres and projections between internal and external capsule is indicated (single arrow and double arrows), and thalamus (dashed circle) where improved contrast to sub structures appear after interpolation to the higher image resolution.

directions, the image volumes represent different views of the same anatomical features and their boundaries. The anatomical features can be bundles of axons ensuring communication between grey matter structures. These fibre projections are spatially related throughout the image space. Because of the spatial coherence of anisotropic pathways, interpolation increases the anatomical information in the individual interpolated DW image volume, improving the reconstruction of the local diffusion tensor. This notion is confirmed by our findings: the use of higher-order B-spline interpolation methods (7th-order) enabled a more correct geometrical representation of the tracts on the sub-grid level compared to using lower order interpolation methods. The higher-order interpolation methods or more advanced interpolation methods in general can infer better the boundaries of anatomical features at a higher image resolution from its neighbourhood.

Each interpolation method has its strengths and weaknesses: The simulations show that using higher order interpolations produced ringing artefacts. A first order interpolation method does not produce such ringing artefact because it is a simple linear fit to the first neighbouring voxels. We observed improvements in the directional contrast of the thinnest tract x when using first order interpolation (appearing more green in the principle direction). For higher order interpolations, it is difficult to decide whether improved anatomical delineation was caused by a better contrast between the true underlying anatomical features at sub-voxel level, a ringing artefact, or a combination of both. Ringing caused by non-related anatomical effects could for example originate from borders between compartments having different T2 relaxation times as observed in $b = 0 \text{ s/mm}^2$ (e.g. between tissue types and liquid). Since the $b = 0 \text{ s/mm}^2$ was uniform in our

simulations, we infer that the ringing observed in the reconstructed FA maps must originate from the true anatomical contrast in the simulated DW image volumes. Alternatively, improved anatomical resolution with higher-order interpolation methods could also be due to the inclusion of a broader neighbourhood for intensity interpolation than 1st order methods. This might particularly apply to noisy and heavily partial-volume effected structures with a local spatial extent in one or two dimensions as fibre tracts. The fibre tracts on the substrates were designed with a two dimensional, sheet-like, extent i.e. repeated tracts in the slice direction. However, in this study we used standard interpolation methods and did not investigated further into optimal interpolation kernel sizes in relation to the spatial extent of anatomical features. Several studies have already shown how regularisation methods using neighbouring information of DWI data prior to fibre reconstruction increase robustness to SNR and improve contrasts between anatomical structures (Arsigny et al., 2006; Haldar et al., 2013; Lam et al., 2013).

More advanced spatial regularisation and super-resolution methods with upsampling might yield even finer and more correct anatomical details of true underlying anatomy (Coupé et al., 2013; Mai et al., 2011; Nedjati-Gilani et al., 2005; Yap et al., 2014). For example, Yap et al. (2014) applied a kind of anisotropic interpolation strategy to acquire DWI based on a directional profiling scheme which encourages interpolation along but not across fibres (Yap et al., 2014). The authors found improved contrast in reconstructed anisotropy maps relative to a 1st-order B-spline. We demonstrated that using model-based interpolation, where the full DT model is interpolated, reveals the finer anatomical details as when interpolating the DWI dataset. Interestingly, we found no significant differences in performance with

DTI indices when comparing DT interpolation to interpolating DWI dataset. However, in Fig. 4 the DT interpolation approach appeared spatially more alike the FA map of the gold standard than when interpolating DWI dataset. The reason could be that the tensor element image volumes have lower contrast compared to the T2-weighted DWIs and could thus be less sensitive to interpolation ringing artefacts. We used the log-Euclidean transformation approach for interpolating the tensor elements (Arsigny et al., 2006), but approaches for interpolating more complex e.g. multi-fibre models might not be straightforward. We revealed, when using both interpolated DWI dataset and DT interpolation, finer anatomical details as in gold standard that are not visible if interpolating the FA map of the low resolution DWI dataset.

With the implementation of the tri-linear interpolation method, Yap et al. (2014) observed a so-called blocking artefact that introduces distortions in the reconstructed image, however we used the implementation in SPM and did not observe any such artefacts, maybe because of a higher SNR. We instead found that the ringing artefact from interpolation could lead to a DT fitting failure. Such failures were typically found for voxels located in high contrast regions as liquid/tissue interfaces in the $b = 0 \text{ s/mm}^2$ as well as in DW image volumes when using low b-values. The fitting problem occurs typically when voxel intensities in $b = 0 \text{ s/mm}^2$ get lower than that of the DW image volume. Reduction of the water signal, multiple b-shells or other basis functions for interpolation with suppressed ringing artefact i.e. windowed Sinc interpolation could potentially recover this problem.

Strong diffusion weighting applied along the fibres can lead to regional signal decay towards the noise floor. Interpolation of noise leads to more continuous images, i.e. an appearing Perlin noise-like effect (Perlin, 1985) with an appearing low frequency structure modulated by the sampling frequency. Since interpolation did not change noise characteristics, we believe that its effect for low SNR is similar to that of DT for original image resolution (Jones and Basser, 2004). It may however be subject to spatial modulation by the Perlin noise-like effect.

When applying interpolation, one should be aware of the inherent limitations and challenges of interpolation methods, as already discussed especially those methods that account for tissue anisotropy (Mai et al., 2011; Yap et al., 2014) and optimize their ability to preserve the correct geometrical features at the highest image resolution (Mai et al., 2011). We successfully applied the interpolation approach on DWI datasets using DTI. The basic principle is expected to be valid for any fibre reconstruction method that is designed for the acquired DWI in angular resolution at original image resolution, but the benefits may vary between methods.

Tractography methods mostly use interpolation to create continuous tensor fields for making the step-wise tracking more robust and precise (Basser et al., 2000; Behrens et al., 2003). However, the interpolation step in tractography is typically applied to the reconstructed directional fibre vector field, and not to the raw DWI dataset simply to avoid the massive data handling (Behrens et al., 2003). However, some diffusion MRI toolboxes today offer interpolation of DWI 'on the fly' in tractography which prevents the need for large stored datasets i.e. Camino (<http://cmic.cs.ucl.ac.uk/camino/>) and MRITrix (<http://www.brain.org.au/software/mritrix/>). A recently introduced Track Density Imaging (TDI) technique is based on the reconstructed fibre-field from acquired DWI datasets (Calamante et al., 2010). This technique does not limit the streamline projections to the grid of the original image resolution as in traditional tractography, but to that of a very high final image resolution. In this way the streamlines themselves act as the 'interpolation method' revealing contrast to appearing finer anatomical details at the higher image resolution.

Sampling factor

Two key factors influence the beneficial effects of interpolating DWI datasets prior to reconstruction. The first factor concerns the relation between the grid size (voxel size) and the size of anatomical structures.

The second factor is related to the interpolation method used. These two factors determine the optimal sampling factor that should be applied during interpolation. Our simulations revealed that a 7th-order B-spline interpolation was found to be optimal and a SF > 16 still provided minor additional information. However, when applied to a high-quality ex vivo data set, the improvement in anatomical resolution visually plateaued at a SF of 8. The difference in optimal SF can be attributed to the fact that the simulated environments were less complex, consisting only of two spatially homogeneous fibre configurations (crossing fibres). In contrast, the brain tissue is much more complex containing spatially heterogeneous structures. Another important aspect is that interpolation cannot resolve anatomical structures that already are poorly represented in the original data. If fibre tracts are coarsely sampled on the grid, interpolation will introduce artefacts due to PVE. This was observed in simulations of curved tracts that appeared piecewise interrupted along the tract after interpolation (Fig. 3) and persisted at higher SFs.

Anatomical structures on the grid

The finer geometrical details revealed by interpolation are generally found in brain regions with complex fibre structures. In the WM, this was most clearly evident at the interface between larger fibre tracts where interpolation resulted in a one-voxel broad stripe of low FA values along the interface between larger orthogonal tracts or tracts that have a low incident angle. Simulations suggested that the stripe indicates PVE due to crossing fibres, and since it gets thinner with higher SF it is a positive effect indicating reduced PVE. More homogeneous WM regions such as the corpus callosum or the corona radiata are characterized by sheet-shaped structures. These homogeneous structures remain largely unaffected by interpolation except at their tract interfaces. While the image contrast in the WM is mainly driven by highly anisotropic structures at WM tract interfaces, the contrast in GM structures comes mainly from a fibre-versus-cell body contrast covering a range of low to medium anisotropy values. Here interpolation made it possible to derive finer anatomical details of GM structures and their orientation from low image resolution data (0.6^3 and 1^3 mm^3), which were not visible in the original image resolution. The finer details appear as an increased contrast between GM regions of high cell density and regions containing many neurites (axons and dendrites). This was observed in layers of the cerebral cortex, hippocampus, cerebellum and thalamus. We speculate that an improved GM contrast will be mostly evident in GM structures with a high fraction of anisotropic structures i.e. neurites. If an anatomical structure (e.g. the folded hippocampal layers) is originally too coarsely sampled (e.g. at 1^3 mm^3 image resolution), interpolation cannot recover the true layered structural contrast that can be obtained without interpolation at higher image resolutions. However, we wish to point out that in such low resolution situations DEC-FA maps from the interpolated DWI dataset actually managed to reveal the true overall folded orientation information of hippocampal layers from the principle direction. Our anatomical findings are in line with our previous work where DEC-FA maps of the fixed pig brain revealed the layered organisation in GM regions as in both the cerebral cortex and the hippocampus (Dyrby et al., 2011). Layered organisation of the living and fixated human brain has also been found with DTI in cerebral cortex (Leuze et al., 2012; McNab et al., 2013) and hippocampus (Shepherd et al., 2007). While Nissl staining revealed far much finer layer details than FA reflecting differences in cell density amongst layers, DEC-FA maps mainly provide information about structural orientation.

When interpolating the lower image resolution ex vivo DWI datasets ($>0.6^3 \text{ mm}^3$), the reconstructed FA maps appeared to have a lower anatomical contrast than the FA maps derived from the original higher resolution DWI dataset. The lower contrast appears as a blurring of the FA map, which emphasizes the larger structures. Such blurring was less prominent in the higher image resolution DWI datasets ($<0.6^3 \text{ mm}^3$). Similar blurring effects were also seen in the interpolated

human DWI dataset when interpolated from 2.3 to 1.15 mm³ voxels with SF of 8. The main source of the blurring effect may be a consequence of the grid size (image resolution) getting too coarse compared to geometrical dimensions of the overall anatomical structures to be sampled, but the blurring effect also comes from the kernel introduced by the interpolation method. Minimal blurring after interpolation was observed in the monkey dataset at an isotropic resolution below 0.6³ mm³. Taking into account the volume ratio between human and monkey being roughly 27 (length × height × width ratio as 3 × 3 × 3) then, we can infer from this information that the corresponding acquired image resolution of the human brain should roughly be less than 1.5³ mm³ to ensure similar minimal blurring effect after interpolation. This, when compared with a 0.5³ mm³ ex vivo monkey dataset. Indeed, such image resolution is too low for today's clinical scanners, but promising new multiplexing techniques have recently been presented allowing clinical scanners to efficiently achieve higher image resolutions while preserving scan time (Feinberg et al., 2010).

Conclusion

The results show that the application of well-established interpolation methods to diffusion weighted imaging datasets acquired in high angular resolution before reconstruction can reveal anatomical details only seen for the higher image resolutions. We combined simulations, high quality ex vivo DWI datasets in various higher image resolutions and classical histology for validating the results. We found in simulations that the tract geometry, and fibre directionality are more correctly reconstructed when using higher order interpolation methods. When interpolation was applied to a typical human DWI dataset, it was concluded based on the ex vivo monkey results, that the acquired image resolution of the human brain today is too coarse compared to the size of the anatomical structures to exploit the full potential of interpolation. Further investigations are needed to test more complex interpolation techniques and get insight into their pros and cons, and to develop ways to better quantify the revealed anatomical details after the reconstruction of interpolated DWI datasets.

Supplementary data to this article can be found online at <http://dx.doi.org/10.1016/j.neuroimage.2014.09.005>.

Acknowledgment

The study was a part of the project "CONNECT" that acknowledges the financial support of the Future and Emerging Technologies (FET) programme within the Seventh Framework Program for Research of the European Commission, under FET-Open grant number: 238292. T.D. was partially funded by a "Grant of Excellence on the Control of Actions" sponsored by Lundbeckfonden (PI: Hartwig Siebner; Grant Nr. R59 A5399).

References

- Alexander, D.C., Hubbard, P.L., Hall, M.G., Moore, E.A., Ptito, M., Parker, G.J., Dyrby, T.B., 2010. Orientational invariance indices of axon diameter and density from diffusion MRI. *NeuroImage* 52, 1374–1389.
- Andersson, J.L.R., Skare, S., Ashburner, J., 2003. How to correct susceptibility distortions in spin-echo echo-planar images: application to diffusion tensor imaging. *NeuroImage* 20, 870–888.
- Arsigny, V., Fillard, P., Pennec, X., Ayache, N., 2006. Log-Euclidean metrics for fast and simple calculus on diffusion tensors. *Magn. Reson. Med.* 56, 411–421.
- Basser, P.J., Mattiello, J., LeBihan, D., 1994. MR diffusion tensor spectroscopy and imaging. *Biophys. J.* 66, 259–267.
- Basser, P.J., Pajevic, S., Pierpaoli, C., Duda, J., Aldroubi, A., 2000. In vivo fiber tractography using DT-MRI data. *Magn. Reson. Med.* 44, 625–632.
- Behrens, T.E.J., Woolrich, M.W., Jenkinson, M., Johansen-Berg, H., Nunes, R.G., Clare, S., Matthews, P.M., Brady, J.M., Smith, S.M., 2003. Characterization and propagation of uncertainty in diffusion-weighted MR imaging. *Magn. Reson. Med.* 50, 1077–1088.
- Burke, M.W., Zangenehpour, S., Boire, D., Ptito, M., 2009. Dissecting the non-human primate brain in stereotaxic space. *J. Vis. Exp.* 1–5.
- Calamante, F., Tournier, J.-D., Jackson, G.D., Connelly, A., 2010. Track-density imaging (TDI): super-resolution white matter imaging using whole-brain track-density mapping. *NeuroImage* 53, 1233–1243.
- Castañó-Moraga, C.A., Rodriguez-Florido, M.A., Alvarez, L., Westin, C.-F., Ruiz-Alzola, J., 2004. Anisotropic interpolation of DT-MRI. *Seventh International Conference on Medical Image Computing and Computer-Assisted Intervention*. Springer, Berlin Heidelberg, pp. 343–350.
- Cook, P.A., B.Y., Nedjati-Gilani, S., Seunarine, K.K., Hall, M.G., Parker, G.J., Alexander, D.C., 2006. Camino: open-source diffusion-MRI reconstruction and processing. *Proceedings of the 14th Scientific Meeting of the International Society for Magnetic Resonance in Medicine*, Seattle, Washington, USA, p. 2759.
- Coupé, P., Manjón, J.V., Chamberland, M., Descoteaux, M., Hiba, B., 2013. Collaborative patch-based super-resolution for diffusion-weighted images. *NeuroImage* 83, 245–261.
- Dyrby, T.B., Baaré, W.F.C., Alexander, D.C., Jelsing, J., Garde, E., Søgaard, L.V., 2011. An ex vivo imaging pipeline for producing high-quality and high-resolution diffusion-weighted imaging datasets. *Hum. Brain Mapp.* 32, 544–563.
- Dyrby, T.B., Sgaard, L.V., Hall, M.G., Ptito, M., Alexander, D.C., 2012. Contrast and stability of the axon diameter index from microstructure imaging with diffusion MRI. *Magn. Reson. Med.* 70, 711–721.
- Feinberg, D.A., Moeller, S., Smith, S.M., Auerbach, E., Ramanna, S., Glasser, M.F., Miller, K.L., Ugurbil, K., Yacoub, E., 2010. Multiplexed echo planar imaging for sub-second whole brain fMRI and fast diffusion imaging. *PLoS One* 5, e15710.
- Greenspan, H., Oz, G., Kiryat, N., Peled, S., 2002 Jun. MRI inter-slice reconstruction using super-resolution. *Magn. Reson. Imaging* 20 (5), 437–446.
- Gudbjartsson, H., Patz, S., 1995. The Rician distribution of noisy MRI data. *Magn. Reson. Med.* 34, 910–914.
- Haldar, J.P., Wedeen, V.J., Nezamzadeh, M., Dai, G., Weiner, M.W., Schuff, N., Liang, Z.P., 2013. Improved diffusion imaging through SNR-enhancing joint reconstruction. *Magn. Reson. Med.* 69, 277–289.
- Jansons, K.M., Alexander, D.C., 2003. Persistent angular structure: new insights from diffusion MRI data. *Dummy version*. *Inf. Process. Med. Imaging* 18, 672–683.
- Jones, D.K., Bassar, P.J., 2004. Squashing peanuts and smashing pumpkins?: how noise distorts diffusion-weighted MR data. *Magn. Reson. Med.* 52, 979–993.
- Kindlmann, G., Ennis, D.B., Whitaker, R.T., Westin, C.F., 2007. Diffusion tensor analysis with invariant gradients and rotation tangents. *IEEE Trans. Med. Imaging* 26, 1483–1499.
- Lam, F., Babacan, S.D., Haldar, J.P., Weiner, M.W., Schuff, N., Liang, Z.P., 2013. Denoising diffusion-weighted magnitude MR images using rank and edge constraints. *Magn. Reson. Med.* 71 (3), 1272–1284.
- Leemans, A., Jones, D.K., 2009. The B-matrix must be rotated when correcting for subject motion in DTI data. *Magn. Reson. Med.* 61, 1336–1349.
- Lehmann, T.M., Gonner, C., Spitzer, K., 1999. Survey: interpolation methods in medical image processing. *IEEE Trans. Med. Imaging* 18, 1049–1075.
- Leuze, C.W.U., Anwander, A., Bazin, P.-L., Dhital, B., Stüber, C., Reimann, K., Geyer, S., Turner, R., 2012. Layer-Specific Intracortical Connectivity Revealed with Diffusion MRI. (*cercor.oxfordjournals.org*).
- Lundell, H., Nielsen, J.B., Ptito, M., Dyrby, T.B., 2011. Distribution of collateral fibers in the monkey cervical spinal cord detected with diffusion-weighted magnetic resonance imaging. *NeuroImage* 56, 923–929.
- Mai, Z., Rajan, J., Verhoeve, M., Sijbers, J., 2011. Robust edge-directed interpolation of magnetic resonance images. *Phys. Med. Biol.* 56, 7287–7303.
- McNab, J.A., Polimeni, J.R., Wang, R., Augustinack, J.C., Fujimoto, K., Stevens, A., Triantafyllou, C., Janssens, T., Farivar, R., Folkert, R.D., Vanduffel, W., Wald, L.L., 2013. Surface based analysis of diffusion orientation for identifying architectonic domains in the in vivo human cortex. *NeuroImage* 69, 87–100.
- Nedjati-Gilani, S., Alexander, D.C., Parker, G.J.M., 2005. Regularized super-resolution for diffusion MRI. *5th IEEE International Symposium on Biomedical Imaging (ISBI 2008)*. IEEE, pp. 875–878.
- Ouchi, H., Yamada, K., Sakai, K., Kizu, O., Kubota, T., Ito, H., Nishimura, T., 2007. Diffusion anisotropy measurement of brain white matter is affected by voxel size: underestimation occurs in areas with crossing fibers. *Am. J. Neuroradiol.* 28, 1102–1106.
- Pajevic, S., Pierpaoli, C., 1999. Color schemes to represent the orientation of anisotropic tissues from diffusion tensor data: application to white matter fiber tract mapping in the human brain. *Magn. Reson. Med.* 42, 526–540.
- Perlin, K., 1985. An image synthesizer. ACM, New York, New York, USA.
- Poot, D.H.J., Jeurissen, B., Bastiaensen, Y., Veraart, J., Van Hecke, W., Parizel, P.M., Sijbers, J., 2012. Super-resolution for multislice diffusion tensor imaging. *Magn. Reson. Med.* 69, 103–113.
- Reese, T.G., Heid, O., Weisskoff, R.M., Wedeen, V.J., 2003. Reduction of eddy-current-induced distortion in diffusion MRI using a twice-refocused spin echo. *Magn. Reson. Med.* 49, 177–182.
- Scherrer, B., Gholipour, A., Warfield, S.K., 2012. Super-resolution reconstruction to increase the spatial resolution of diffusion weighted images from orthogonal anisotropic acquisitions. *Med. Image Anal.* 16, 1465–1476.
- Shepherd, T.M., Ozarslan, E., Yachnis, A.T., King, M.A., Blackband, S.J., 2007. Diffusion Tensor Microscopy Indicates the Cytoarchitectural Basis for Diffusion Anisotropy in the Human Hippocampus. (*ajnr.org*).
- Smith, S.M., Jenkinson, M., Woolrich, M.W., Beckmann, C.F., Behrens, T.E.J., Johansen-Berg, H., Bannister, P.R., De Luca, M., Drobniak, I., Flitney, D.E., Niacy, R.K., Saunders, J., Vickers, J., Zhang, Y., De Stefano, N., Brady, J.M., Matthews, P.M., 2004. Advances in functional and structural MR image analysis and implementation as FSL. *NeuroImage* 23, S208–S219.
- Yap, P.-T., An, H., Chen, Y., Shen, D., 2014. Fiber-driven resolution enhancement of diffusion-weighted images. *NeuroImage* 84, 939–950.
- Zhang, H., Dyrby, T.B., Alexander, D.C., 2011. Axon diameter mapping in crossing fibers with diffusion MRI. *Med. Image Comput. Comput. Assist. Interv.* 14, 82–89.
- Zhang, H., Schneider, T., Wheeler-Kingshott, C.A., Alexander, D.C., 2012. NODDI: practical in vivo neurite orientation dispersion and density imaging of the human brain. *NeuroImage* 61, 1000–1016.